Advances in Computational Modelling of Multi-Physics in Particle-Fluid Systems

Y.T. Feng, K. Han and D.R.J. Owen

Abstract The current work presents the recent advances in computational modelling strategies for effective simulations of multi physics involving fluid, thermal and magnetic interactions in particle systems. The numerical procedures presented comprise the Discrete Element Method for simulating particle dynamics; the Lattice Boltzmann Method for modelling the mass and velocity field of the fluid flow; the Discrete Thermal Element Method and the Thermal Lattice Boltzmann Method for solving the temperature field. The coupling of the fields is realised through hydrodynamic and magnetic interaction force terms. Selected numerical examples are provided to illustrate the applicability of the proposed approach.

1 Introduction

In recent years the modelling of coupled field problems, in which two or more physical fields contribute to the system response, has become a focus of major research activity. Among them, the quantitative study of fluid, thermal and magnetic interactions in particulate systems encountered in many engineering applications is of fundamental importance. For instance, the mineral recovery operation in the mining industry employs a suction process to extract rock fragments from the ocean or river bed. The computational modelling of this particle transport problem requires a fluid-particle interaction simulation. The motion of the particles is driven collectively by the gravity and the hydrodynamic forces exerted by the fluid, and may also be altered by the interaction between the particles. On the other hand, the fluid flow pattern can be greatly affected by the presence of the particles, and is often of a turbulent nature. In the nuclear industry, the process of a pebble bed nuclear reactor essentially involves the forced flow of gas through uranium enriched spheres that

Y.T. Feng · K. Han · D.R.J. Owen
Civil and Computational Engineering Centre, School of Engineering, Swansea University, Swansea SA2 8PP, UK; e-mail: y.feng@swansea.ac.uk

are cyclically fed through a concentric column in order to extract thermal energy. In this situation, the introduction of additional field, thermal (heat transfer between the moving particles in the form of conduction, convection, and radiation, as well as transfer of heat to the gas stream), poses even more computational challenges. Another example is the modelling of magnetorheological fluids (MR fluids). An MR fluid is a type of smart fluid, which consists of micron-sized magnetizable particles dispersed in a non-magnetic carrier fluid. In the absence of a magnetic field, the rheological behaviour of an MR fluid is basically that of the carrier fluid, except that the suspended magnetizable particles makes the fluid 'thicker'. When subjected to an external magnetic field, the particles become magnetized and acquire a dipole moment. Due to magnetic dipolar interactions, the particles line up and form chain-like structures in the direction of the applied field. This change in the suspension microstructure significantly alters the rheological properties of the fluid. To model the particle chain formation and the rheological properties of the MR fluid under an applied magnetic field, the magnetic, hydrodynamic and contact interactions should be fully resolved.

The fundamental physical phenomena involved in these systems are generally not well understood and often described in an empirical fashion, mainly due to the intricate complexity of the hydrodynamic, thermodynamic and magnetic interactions exhibited and the non-existence of high-fidelity modelling capability.

The Discrete Element Method [5], among other discontinuous methodologies, has become a promising numerical tool capable of simulating problems of a discrete or discontinuous nature. In the framework of the Discrete Element Method, a discrete system is considered as an assembly of individual discrete objects which are treated as rigid and represented by discrete elements as simple geometric entities. The dynamic response of discrete elements depends on the interaction forces which can be short-ranged, such as mechanical contact, and/or medium-ranged, such as attraction forces in liquid bridges, and obey Newton's second law of motion. By tracking the motion of individual discrete elements and handling their interactions, the dynamic behaviour of a discrete system can be simulated.

Conventional computational fluid dynamic methods have limited success in simulating particulate flows with a high number of particles due to the need to generate new, geometrically adapted grids, which is a very time-consuming task especially in three-dimensional situations [10]. In contrast, the Lattice Boltzmann Method [2, 36] overcomes the limitations of the conventional numerical methods by using a fixed, non-adaptive (Eulerian) grid system to represent the flow field. In particular, it can efficiently model fluid flows in complex geometries, as is the case of particulate flow under consideration. A rich publication in recent years (see, for instance, [1, 4, 10, 13, 15, 16, 21, 28, 29, 33] and the references therein) has proved the effectiveness of the method.

If an additional field, thermal, is introduced to a particulate system, the Thermal Lattice Boltzmann Method [25] may be employed to model heat transfer between particles and between particles and the surrounding fluid. Our numerical tests show, however, that the Thermal Lattice Boltzmann Method is not efficient for simulating heat conduction in particles. For this reason, a novel numerical scheme, termed

the Discrete Thermal Element Method [14] is put forward. In this approach, each particle is treated as an individual element with the number of (temperature) unknowns equal to the number of particles that it is in contact with. The element thermal conductivity matrix can be very effectively evaluated and is entirely dependent on the contact characteristics. This new element shares the same form and properties with its conventional thermal finite element counterpart. In particular, the entire solution procedure can follow exactly the same steps as those involved in the finite element analysis. Unlike finite elements or other numerical techniques, no discretisation errors are involved in the Discrete Thermal Element Method. The numerical validation against the finite element solution indicates that the solution accuracy of this scheme is reasonable and highly efficient in particular.

The interaction problems considered is often of a dynamic and transient nature. Although the Discrete Thermal Element Method is capable of modelling the steady-state heat conduction in large particulate systems efficiently, it is not trivial to be extended to transient situations. Meanwhile, its formulation is not compatible with that of the Discrete Element Method which accounts for particle-particle interactions. Therefore the Discrete Thermal Element Method needs to be modified to realise thermal-particle coupling. The pipe-network model is such a modification [15], in which each particle is replaced by a thermal pipe-network connecting the particle's centre with each contact zone associated with the particle.

For numerical modelling of magnetorheological fluids, in addition to the above numerical techniques, the magnetic forces formed between magnetized particles under an externally applied magnetic field need to be properly accounted for. This turns out not to be an easy issue since the mutual

The objective of this work is to present our recent developments [13–16, 23, 24] on all essential computational procedures for the effective modelling of the above mentioned multi-physics problems involving fluid, thermal and/or magnetic interactions in particulate systems. In what follows, the basic formulations of the Discrete Element Method, the Lattice Boltzmann Method, the Discrete Thermal Element Method, the magnetic interactions and the coupling techniques, will be outlined. Selected numerical examples are provided to illustrate the applicability of the proposed approach.

2 Particle-Particle Interactions – Discrete Element Approach

Interactions between the moving particles are modelled by the Discrete Element Method [5], in which each discrete object is treated as a geometrically simplified entity that interacts with other discrete objects through boundary contact. At each time step, objects in contact are identified with a contact detection algorithm; and the contact forces are evaluated based on appropriate interaction laws. The motion of each discrete object is governed by Newton's second law of motion. A set of governing equations is built up and integrated with respect to time, to update each

object's position, velocity and acceleration. The main building blocks of the discrete element procedure are described as follows.

2.1 Representation of Discrete Objects

In the Discrete Element Method, discrete objects are treated as rigid and represented either by regular geometric shapes, such as disks, spheres and superquadrics, or by irregular geometric shapes, such as polygons, polyhedrons, clustering or clumping of regular shapes to form compound shapes.

Circular and spherical elements are the most used discrerete elements due to their geometric simplicity, smooth and continuous boundary. Contact resolution for this type of element is therefore trivial and computationally efficient. However, idealising materials such as grains and concrete aggregates as perfect disks (or spheres) is not always realistic and may not produce correct dynamic behaviour. One of the reasons is that circular and spherical elements cannot provide resistance to rolling motion. This has led to the introduction of more sophisticated elements to represent the discrete system more realistically.

Contrary to the circular and spherical elements where only the radius can be modified, polygonal elements (polygons or polyhedrons) offer increased flexibility in terms of shape variation. Since the boundary of this type of element is not smooth, some complex situations such as corner/corner contact, often arise in the contact resolution.

Higher order discrete elements can be used, such as superquadrics and hyperquadrics as proposed in [37], which may represent many simple geometric entities (for instance, disk, sphere, ellipse and ellipsoid) within the framework. However, this mathematical elegancy may be offset by the expensive computation involved in the contact resolution.

Preparation of an initial packing configuration of particles is a very important issue both practically and numerically. There is only limited work reported. See [8, 9] for a very effective packing of disks/ploygons, and for [19] for spheres.

2.2 Contact Detection

In the discrete element simulation of problems involving a large number of discrete objects, as much as 60–70% of the computational time could be spent in detecting and tracking the contact between discrete objects. Due to a large diversity of object shapes, many efficient contact processing algorithms often adopt a two-phase solution strategy. The first phase, termed contact detection or global search, identifies the discrete objects which are considered as potential contactors of a given object. The second phase, termed contact resolution or local search, resolves the details of the contact pairs based on their actual geometric shapes.

Some search algorithms used in general computing technology and computer graphics have been adopted for this purpose. Algorithms such as bucket sorting, heap sorting, quick sorting, binary tree and quadrant tree data structure all originated from general computing algorithms. However, applications of these algorithms in discrete element codes need modifications to meet the needs of particular discrete element body representations and the kinematic resolution.

For the detection of potential contact between a large number of discrete elements, a spatial search algorithm based on space-cell subdivision and incorporating a tree data storage structure possesses significant computational advantages. For instance, the augmented spatial digital tree [6] is a spatial binary tree based contact detection algorithm. It uses the lower corner vertex to represent a rectangle in a binary spatial tree, with the upper corner vertex serving as the augmented information. The algorithm is insensitive to the size distributions of the discrete objects. Numerical experiments in [6] indicate that this search algorithm can reduce the CPU requirement of a contact detection from an originally demanding level down to a more acceptable proportion of the computing time.

Another type of the contact detection algorithms is the so-called cell based search [31, 32]. The main procedures in these algorithms involve: (1) dividing the domain that the discrete objects occupy into regular grid cells; (2) mapping each discrete object to one of the grid cells; and (3) for each discrete object in a cell, checking for possible contacts with other objects in the same cell and in the neighbouring cells. Provided the number of cell columns and rows is significantly less than the number of discrete objects, it can be proved that the memory requirement for the dynamic cell search algorithm is $O(N)$. Also for a fixed cell size the computational time T_{op} may be expressed as

$$T_{op} = O(N + \epsilon)$$

where ϵ represents the costs associated with the maintenance of various lists used in the algorithm. Numerical tests conducted in [22] show that the dynamic cell search algorithm is even more efficient than the tree based search algorithms for large scale problems.

2.3 Contact Resolution

The identified pairs with potential contact are then kinematically resolved based on their actual shapes. The contact forces are evaluated according to certain constitutive relationship or appropriate physically based interaction laws. In general, the interaction laws describe the relationship between the overlap and the corresponding repulsive force of a contact pair. For rigid discrete elements, the interaction laws may be developed on the basis of the physical phenomena involved. The Hertz normal contact model that governs elastic contact of two spheres (assumed rigid in discrete element modelling) in the normal direction is such an example, in which the normal contact force, F_n, and the contact overlap, δ, has the following relation

$$F_n = \frac{4E^*\sqrt{(R^*)}}{3}\delta^{3/2} \tag{1}$$

where

$$\frac{1}{E^*} = \frac{1 - \nu_1^2}{E_1} + \frac{1 - \nu_2^2}{E_2}$$

$$\frac{1}{R^*} = \frac{1}{R_1} + \frac{1}{R_2}$$

with R_1 and R_2 being the radii; E_1, E_2, and ν_1, ν_2 are the elastic properties (Young's modulus and Poisson's ratio) of the two spheres.

For irregularly shaped particles, such as polygons and polyhedra, the contact interaction models can be an serious issue where the normal direction may not be uniquely defined. Energy based contact models, proposed in [10] for polygons and [11] for polyhedra, provide an elegant solution to the problem. An application to superquadrics is proposed in [20].

For 'wet' particles the interaction laws may include the effects of a liquid bridge. In other cases, adhesion may be considered.

Energy dissipation due to plastic deformation, heat loss and material damping *etc* during contact is taken into account by adding a viscous damping term in the governing equation.

Friction is one of the fundamental physical phenomena involved in particulate systems. Although the search for a quantitative understanding of the features of friction has been in progress for several centuries, a universally accepted friction model has not yet been achieved. One difficulty is associated with the nature of the friction force near zero relative velocity, where a strong nonlinear behaviour is exhibited. The classic Coulomb friction law is usually employed in engineering applications for its simplicity. The discontinuous nature of the friction force in this model, however, imposes some numerical difficulties when the relative sliding velocity reverses its direction and/or during the transition from sliding (sticking) to sticking (sliding). The difficulties are usually circumvented by artificially introducing a 'transition zoneŠ which smears the discontinuity in the numerical computation. Nevertheless, the suitability of any friction model should be carefully examined and the associated numerical issues fully investigated in order to correctly capture the physical phenomena involved. Proper considering rolling friction is another challenging issue and many numerical issues remain outstanding [7].

A comprehensive study of the contact interaction laws can be found in [17, 18].

2.4 Governing Equations and Time Stepping

The motion of the discrete objects is governed by Newton's second law of motion as

$$\begin{cases} \mathbf{M}\ddot{\mathbf{u}} + \mathbf{C}_d\dot{\mathbf{u}} = \mathbf{F}_c \\ J\ddot{\theta} = \mathbf{T}_c \end{cases} \tag{2}$$

where $\mathbf{M}$ and $\mathbf{C}_d$ are respectively the mass and damping matrices of the system, $\mathbf{u}$, $\dot{\mathbf{u}}$ and $\ddot{\mathbf{u}}$ are respectively the displacement, velocity and acceleration vectors, J is the moment of inertia, $\ddot{\theta}$ the angular acceleration, $\mathbf{F}_c$ and $\mathbf{T}_c$ denote the contact force and torque, respectively.

The configuration of the entire discrete system is evolved by employing an explicit time integration scheme. With this scheme, no global stiffness matrix needs to be formed and inverted, which makes the operations at each time step far less computationally intensive. However, any explicit time integration scheme is only conditionally stable. For a linear system the critical time step can be evaluated as

$$\Delta t_{cr} = \frac{2}{\omega_{\max}} \tag{3}$$

where $\omega_{\max}$ is the maximum eigenvalue of the system. However, the above result may not be valid since a contact system is generally nonlinear, as is demonstrated in [12]. To ensure a stable and reasonably accurate solution, the critical time step chosen should be much smaller than the value given in Eq. (3).

3 Fluid-Particle Interactions

The interaction between fluid and particles is solved by a coupled technique: using the Lattice Boltzmann Method to simulate the fluid field, and the Discrete Element Method to model particle dynamics. The hydrodynamic interactions between fluid and particles are realised through an immersed boundary condition. The solution procedures are outlined as follows.

3.1 The Lattice Boltzmann Method

In the Lattice Boltzmann Method, the problem domain is divided into regular lattice nodes. The fluid is modelled as a group of fluid particles that are allowed to move between lattice nodes or stay at rest. During each discrete time step of the simulation, fluid particles move to the nearest lattice node along their directions of motion, where they 'collide' with other fluid particles that arrive at the same node. By tracking the evolution of fluid particle distributions, the macroscopic variables, such as velocity and pressure, of the fluid field can be conveniently calculated from its first two moments.

The lattice Boltzmann equation with a single relaxation time for the collision operator is expressed as

$$f_i(\mathbf{x} + \mathbf{e}_i \Delta t, t + \Delta t) - f_i(\mathbf{x}, t) = -\frac{1}{\tau} \left[f_i(\mathbf{x}, t) - f_i^{eq}(\mathbf{x}, t) \right] \tag{4}$$

where f_i is the density distribution function of the fluid particles with discrete velocity $\mathbf{e}_i$ along the i-th direction; f_i^{eq} is the equilibrium distribution function; and τ is the relaxation time which controls the rate of approach to equilibrium. The left-hand side of Eq. (4) denotes a streaming process for fluid particles while the right-hand side models collisions through relaxation.

In the widely used D2Q9 model [33], the fluid particles at each node move to their eight immediate neighbouring nodes with discrete velocities $\mathbf{e}_i$ ($i = 1, \ldots, 8$). The equilibrium distribution functions f_i^{eq} depend only on the fluid density, ρ, and velocity, $\mathbf{v}$, which are defined in D2Q9 model as

$$\begin{cases} f_0^{eq} = \rho \left(1 - \dfrac{3}{2c^2} \mathbf{v} \cdot \mathbf{v} \right) \\ f_i^{eq} = w_i\, \rho \left(1 + \dfrac{3}{c^2} \mathbf{e}_i \cdot \mathbf{v} + \dfrac{9}{2c^4} (\mathbf{e}_i \cdot \mathbf{v})^2 - \dfrac{3}{2c^2} \mathbf{v} \cdot \mathbf{v} \right) \quad (i = 1, \ldots, 8) \end{cases} \tag{5}$$

in which $c = \Delta x / \Delta t$ is the lattice speed with Δx and Δt being the lattice spacing and time step, respectively; w_i is the weighting factor with $w_0 = 4/9$, $w_{1-4} = 1/9$, $w_{5-8} = 1/36$.

The macroscopic fluid variables, density ρ and velocity $\mathbf{v}$, can be recovered from the distribution functions as

$$\rho = \sum_{i=0}^{8} f_i, \qquad \rho \mathbf{v} = \sum_{i=1}^{8} f_i\, \mathbf{e}_i \tag{6}$$

The fluid pressure field p is determined by the following equation of state:

$$p = c_s^2 \rho \tag{7}$$

where c_s is termed the fluid speed of sound and is related to the lattice speed c by

$$c_s = c/\sqrt{3} \tag{8}$$

The kinematic viscosity, ν, of the fluid is implicitly determined by the model parameters, Δx, Δt and τ as

$$\nu = \frac{1}{3} \left(\tau - \frac{1}{2} \right) \frac{\Delta x^2}{\Delta t} = \frac{1}{3} \left(\tau - \frac{1}{2} \right) c\, \Delta x \tag{9}$$

which indicates that the selection of these three parameters should be correlated to achieve a correct fluid viscosity.

It can be proved that the lattice Boltzmann equation (4) recovers the incompressible Navier–Stokes equations to the second order in both space and time [2], which is the theoretical foundation for the success of the Lattice Boltzmann Method for modelling general fluid flow problems. However, since it is obtained by the linearised expansion of the original kinetic theory based Boltzmann equation, Eq. (4) is only valid for small velocities, or small 'computational' Mach number defined by

$$M_a = \frac{v_{\max}}{c} \tag{10}$$

where $v_{\max}$ is the maximum simulated velocity in the flow.

Generally smaller Mach number implies more accurate solution. It is therefore required that

$$M_a \ll 1 \tag{11}$$

i.e., the lattice speed c should be sufficiently larger than the maximum fluid velocity to ensure a reasonably accurate solution.

3.2 Incorporating Turbulence Model in the Lattice Boltzmann Equation

As many fluid-particle interaction problems are turbulent in nature, a turbulence model should be incorporated into the lattice Boltzmann equation (4).

The Large Eddy Simulation, amongst other turbulence models, solves large scale turbulent eddies directly but the smaller scale eddies using a sub-grid model. The separation of these scales is achieved through the filtering of the Navier–Stokes equations, from which the solutions to the resolved scales are directly obtained. Unresolved scales can be modelled by, for instance, the Smagorinsky sub-grid model [34] that assumes that the Reynolds stress tensor is dependent only on the local strain rate.

Yu et al. [38] proposed to incorporate the Large Eddy Simulation in the lattice Boltzmann equation by including the eddy viscosity as

$$\tilde{f}_i(\mathbf{x} + \mathbf{e}_i \Delta t, t + \Delta t) = \tilde{f}_i(\mathbf{x}, t) - \frac{1}{\tau_*} \left[\tilde{f}_i(\mathbf{x}, t) - \tilde{f}_i^{eq}(\mathbf{x}, t) \right] \tag{12}$$

where $\tilde{f}_i$ and $\tilde{f}_i^{eq}$ denote the distribution function and the equilibrium distribution function at the resolved scale, respectively. The effect of the unresolved scale motion is modelled through an effective collision relaxation time scale τ_t. Thus in Eq. (12) the total relaxation time equals

$$\tau_* = \tau + \tau_t$$

where τ and τ_t are respectively the relaxation times corresponding to the true fluid viscosity v and the turbulence viscosity v_* defined by a sub-grid turbulence model. Accordingly, v_* is given by

$$v_* = v + v_t = \frac{1}{3} \left(\tau_* - \frac{1}{2} \right) c^2 \Delta t = \frac{1}{3} \left(\tau + \tau_t - \frac{1}{2} \right) c^2 \Delta t$$

$$v_t = \frac{1}{3} \tau_t c^2 \Delta t$$

With the Smagorinsky model, the turbulence viscosity v_t is explicitly calculated from the filtered strain rate tensor $\tilde{S}_{ij} = (\partial_j \tilde{u}_i + \partial_i \tilde{u}_j)/2$ and a filter length scale (which is equal to the lattice spacing Δx) as

$$v_t = (S_c \, \Delta x)^2 \hat{S} \tag{13}$$

where S_c is the Smagorinsky constant; and $\hat{S}$ the characteristic value of the filtered strain rate tensor $\tilde{S}$

$$\hat{S} = \sqrt{\sum_{i,j} \tilde{S}_{ij} \tilde{S}_{ij}}$$

An attractive feature of the model is that $\tilde{S}$ can be obtained directly from the second-order moments, $\tilde{Q}$, of the non-equilibrium distribution function

$$\tilde{S} = \frac{\tilde{Q}}{2\rho S_c \tau_*} \tag{14}$$

in which $\tilde{Q}$ can be simply computed by the filtered density functions at the lattice nodes

$$\tilde{Q}_{ij} = \sum_{k=1}^{8} e_{ki} e_{kj} (\tilde{f}_k - \tilde{f}_k^{eq}) \tag{15}$$

where e_{ki} is the k-th component of the lattice velocity $\mathbf{e}_i$. Consequently

$$\hat{S} = \frac{\hat{Q}}{2\rho S_c \tau_*} \tag{16}$$

with $\hat{Q}$ the filtered mean momentum flux computed from $\tilde{Q}$

$$\hat{Q} = \sqrt{2 \sum_{i,j} \tilde{Q}_{ij} \tilde{Q}_{ij}} \tag{17}$$

3.3 Hydrodynamic Forces for Fluid-Particle Interactions

The modelling of the interaction between fluid and particles requires a physically correct 'no-slip' velocity condition imposed on their interface. In other words, the fluid adjacent to the particle surface should have identical velocity as that of the particle surface.

Ladd [28] proposes a modification to the bounce-back rule so that the movement of a solid particle can be accommodated. This approach provides a relationship of the exchange of momentum between the fluid and the solid boundary nodes. It also assumes that the fluid fills the entire volume of the solid particle, or in other words, the particle is modelled as a 'shell' filled with fluid. As a result, both solid and fluid

nodes on either side of the boundary surface are treated in an identical fashion. It has been observed, however, that the computed hydrodynamic forces may suffer from severe fluctuations when the particle moves across the grid with a large velocity. This is mainly caused by the stepwise representation of the solid particle boundary and the constant changing boundary configurations.

To circumvent the fluctuation of the computed hydrodynamic forces with the modified bounce-back rule, Noble and Torczynski [30] proposed an immersed moving boundary method. In this approach, a control volume is introduced for each lattice node that is a $\Delta x \times \Delta x$ square around the node, as illustrated by the shadow area in Figure 1a. Meanwhile, a local fluid to solid ratio γ is defined, which is the volume fraction of the nodal cell covered by the particle as shown in Figure 1b.

The lattice Boltzmann equation for those lattice nodes (fully or partially) covered by a particle is modified to enforce the 'no-slip' velocity condition as

$$f_i(\mathbf{x} + \mathbf{e}_i \Delta t, t + \Delta t) = f_i(\mathbf{x}, t) - \frac{1}{\tau}(1 - \beta)\left[f_i(\mathbf{x}, t) - f_i^{eq}\right] + \beta f_i^m \qquad (18)$$

where β is a weighting function depending on the local fluid/solid ratio γ; and f_i^m is an additional term that accounts for the bounce back of the non-equilibrium part of the distribution function, computed by the following expressions:

$$\begin{cases} \beta = \frac{\gamma(\tau - 0.5)}{(1 - \gamma) + (\tau - 0.5)} \\ f_i^m = f_{-i}(\mathbf{x}, t) - f_i(\mathbf{x}, t) + f_i^{eq}(\rho, \mathbf{v}_b) - f_{-i}^{eq}(\rho, \mathbf{v}) \end{cases} \qquad (19)$$

where $-i$ denotes the opposite direction of i.

The total hydrodynamic forces and torque exerted on a particle over n particle-covered nodes are summed up as

$$\mathbf{F}_f = c \, \Delta x \left[\sum_n \left(\beta_n \sum_i f_i^m \mathbf{e}_i \right) \right] \qquad (20)$$

$$\mathbf{T}_f = c \, \Delta x \left[\sum_n (\mathbf{x} - \mathbf{x}_c) \times \left(\beta_n \sum_i f_i^m \mathbf{e}_i \right) \right] \qquad (21)$$

where $\mathbf{x}_c$ is the coordinate of the particle center.

With this approach, the computed hydrodynamic forces are sufficiently smooth, which is also confirmed in our previous numerical tests [13, 21].

3.4 Fluid and Particle Coupling

Fluid and particle coupling at each time step is realised by first computing the fluid solution, and then updating the particle positions through the integration of the equations of motion given by
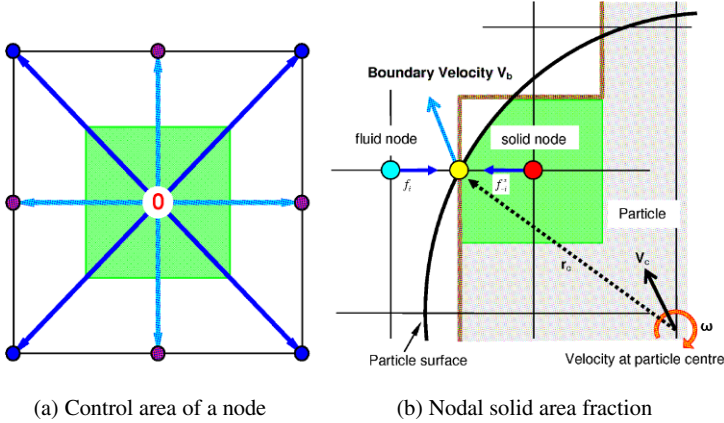
(a) Control area of a node   (b) Nodal solid area fraction

Fig. 1 Immersed boundary scheme of Noble and Torczynski

$$\begin{cases} m\mathbf{a} + c_d\mathbf{v} = \mathbf{F}_c + \mathbf{F}_f + m\mathbf{g} \\ J\ddot{\theta} = \mathbf{T}_c + \mathbf{T}_f \end{cases} \tag{22}$$

where m and J are respectively the mass and the moment of inertia of the particle; $\ddot{\theta}$ the angular acceleration; $\mathbf{g}$ the gravitational acceleration if considered; $\mathbf{F}_f$ and $\mathbf{T}_f$ are respectively the hydrodynamic force and torque; $\mathbf{F}_c$ and $\mathbf{T}_c$ denote the contact force and torque from other particles and/or boundary walls; c_d is a damping coefficient and the term $c_d\mathbf{v}$ represents a viscous force that accounts for the effect of all possible dissipation forces in the system. The static buoyancy force of the fluid is taken into account by reducing the gravitational acceleration to $(1 - \rho/\rho_s)\,\mathbf{g}$, where ρ_s is the density of a particle.

This dynamic equation governing the evolution of the system can be solved by the central difference scheme. Some important computational issues regarding the solution are briefly discussed as follows:

1. *Subcycling time integration.* There are two time steps used in the coupled procedure, Δt for the fluid flow and Δt_p for the particles. Since Δt_p is generally smaller than Δt, it has to be reduced to Δt_s so that the ratio between Δt and Δt_s is an integer n_s:

$$\Delta t_s = \frac{\Delta t}{n_s} \qquad (n_s = \lceil \Delta t/\Delta t_p \rceil + 1) \tag{23}$$

where $\lceil \cdot \rceil$ denotes an integer round-off operator. This basically gives rise to a so-called subcycling time integration for the discrete element part; in one step of the fluid computation, n_s sub-steps of integration are performed for Eq. (22) using the time step Δt_s; whilst the hydrodynamic forces $\mathbf{F}_f$ and $\mathbf{T}_f$ are kept unchanged during the subcycling.

2. *The dynamic equation in the lattice coordinate system.* Since the lattice Boltzmann equation is implemented in the lattice coordinate system in this work, the dynamic equation (22) should be implemented in the same way. It can be de-

rived that in the lattice coordinate system Eq. (22) takes the form of

$$\bar{m}\bar{\mathbf{a}} + \bar{c}_d\bar{\mathbf{v}} = \bar{\mathbf{F}}_c + \bar{\mathbf{F}}_f + \bar{m}\bar{\mathbf{g}} \tag{24}$$

where

$$\begin{cases} \bar{m} = m/\rho_s\Delta x^2 & \bar{\mathbf{v}} = \mathbf{v}/c \\ \bar{\mathbf{a}} = \mathbf{a}\Delta t/c; & \bar{\mathbf{g}} = \mathbf{g}\Delta t/c \\ \bar{c}_d = c\Delta x c_d; & \bar{\mathbf{F}}_t = \mathbf{F}_t/(\rho_0 c^2\Delta x) \end{cases}$$

4 Thermal-Particle Interactions

4.1 Convective Heat Transfer

If an additional field, *thermal*, exists, the Thermal Lattice Boltzmann Method is adopted to account for heat exchange between particles and between particles and the surrounding fluid. In the double-population model [25] , in addition to the evolution equation for fluid flow (Eq. (4)), an internal energy distribution function is also introduced to solve thermodynamics, as described by the following evolution equation:

$$\bar{g}_i(\mathbf{x}+\mathbf{e}_i\Delta t, t+\Delta t) - \bar{g}_i(\mathbf{x}, t) = -\frac{1}{\tau_g + 0.5}\left[\bar{g}_i(\mathbf{x}, t) - g_i^{eq}(\mathbf{x}, t)\right] - \frac{\tau_g}{\tau_g + 0.5} f_i Z_i \tag{25}$$

where

$$\bar{f}_i = f_i + \frac{0.5}{\tau_f}(f_i - f_i^{eq}) \tag{26}$$

$$\bar{g}_i = g_i + \frac{0.5}{\tau_g}(g_i - g_i^{eq}) + \frac{\Delta t}{2} f_i Z_i \tag{27}$$

in which g_i is the internal energy distribution function with discrete velocity $\mathbf{e}_i$ along the i-th direction; g_i^{eq} is the corresponding equilibrium distribution function; τ_g is the internal energy relaxation time which controls the rate of change to equilibrium.

The term $Z_i = (\mathbf{e}_i - \mathbf{v}) \cdot [\partial\mathbf{v}/\partial t + (\mathbf{e}_i \cdot \nabla)\mathbf{v}]$ represents the effect of viscous heating and can be expressed as

$$Z_i = \frac{(\mathbf{e}_i - \mathbf{v}) \cdot [\mathbf{v}(\mathbf{x}+\mathbf{e}_i\Delta t, t+\Delta t) - \mathbf{v}(\mathbf{x}, t)]}{\Delta t} \tag{28}$$

For gas flow, the lattice speed c can be defined as

$$c = \sqrt{3RT_m}$$

where R is the gas constant and T_m the average temperature.

The internal energy equilibrium distribution functions g_i^{eq} are defined in the D2Q9 model as

$$
\begin{cases}
g_0^{eq} = w_0\,\rho\epsilon\left[-\dfrac{3(\mathbf{v}\cdot\mathbf{v})}{2c^2}\right] \\[2mm]
g_i^{eq} = w_i\,\rho\epsilon\left[\dfrac{3}{2}+\dfrac{3(\mathbf{e}_i\cdot\mathbf{v})}{2c^2}+\dfrac{9(\mathbf{e}_i\cdot\mathbf{v})^2}{2c^4}-\dfrac{3(\mathbf{v}\cdot\mathbf{v})}{2c^2}\right] & (i=1,2,3,4) \\[2mm]
g_i^{eq} = w_i\,\rho\epsilon\left[3+\dfrac{6(\mathbf{e}_i\cdot\mathbf{v})}{c^2}+\dfrac{9(\mathbf{e}_i\cdot\mathbf{v})^2}{2c^4}-\dfrac{3(\mathbf{v}\cdot\mathbf{v})}{2c^2}\right] & (i=5,6,7,8)
\end{cases} \quad (29)
$$

in which w_i are the weighting factors with the same values as defined in Section 3.1; and $\rho\epsilon$ denotes the internal energy.

The internal energy per unit mass ϵ and heat flux q can be calculated from the zeroth and first order moments of the distribution functions as

$$
\rho\epsilon = \sum \bar{g}_i - \frac{\Delta t}{2}\sum f_i Z_i; \quad q = \left(\sum \mathbf{e}_i \bar{g}_i - \rho\epsilon\mathbf{v} - \frac{\Delta t}{2}\sum \mathbf{e}_i f_i Z_i\right)\frac{\tau_g}{\tau_g + 0.5}
\tag{30}
$$

To evaluate the convective heat exchange between a solid particle and the surrounding fluid, the following approach is proposed in this work.

Assume that a solid particle is mapped onto the lattice by a set of lattice nodes. The nodes on the boundary of the solid region are termed boundary nodes. If i is a link (or direction) between a boundary node and a fluid node, the convective heat exchange between the solid particle and the surrounding fluid can be evaluated as

$$
q = \sum_i [g_{-i}(\mathbf{x}, t) - g_i(\mathbf{x}, t_+)]
\tag{31}
$$

where $g_i(\mathbf{x}, t_+)$ denotes the post collision distribution at the boundary node $\mathbf{x}$, and $-i$ is the opposite direction of i.

Our numerical tests show that the Thermal Lattice Boltzmann Method can model natural or forced convection in particulate systems well, but is not efficient to simulate heat conduction between particles, particularly for systems comprising a large number of particles. For this reason, a novel numerical approach, termed the Discrete Thermal Element Method [14], is proposed, which is outlined in the following.

4.2 Conductive Heat Transfer in Particles

Consider a circular particle of radius R in a particle assembly that is in contact with n neighboring particles, as shown in Figure 2a, in which heat is conducted only through the n contact zones on the boundary of the particle, and the rest of the particle boundary is fully insulated. A polar coordinate system (r, θ) is established with the origin set at the centre of the particle. Each contact zone (assumed to be an arc) can be described by the position angle θ and the contact angle α in Figure 2b. In general situations the position angles are well spaced along the boundary and the

(a) A circular particle in an assembly

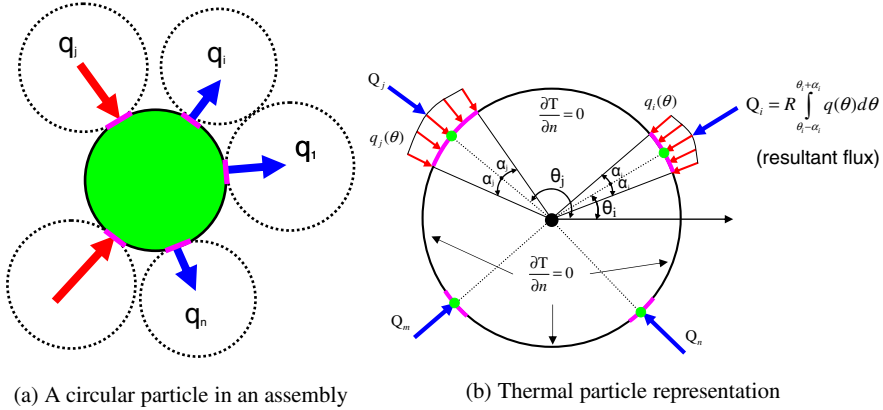(b) Thermal particle representation

Fig. 2 Heat conduction in a simple particle system

contact angles α_i are small. The position and contact angles of the n contact zones constitute the local element (contact) configuration of the particle. Furthermore, if the heat flux along the i-th contact zone is described by a (local) continuous function $q_i(\theta)$, then the heat flux on the boundary of the particle can be represented as

$$q(\theta) = \begin{cases} q_i(\theta - \theta_i) & \theta_i - \alpha_i \leq \theta \leq \theta_i + \alpha_i \quad (i = 1, \ldots, n) \\ 0 & \text{otherwise} \end{cases} \tag{32}$$

The heat flux equilibrium in the particle requires

$$\int_0^{2\pi} q(\theta)d\theta = 0 \tag{33}$$

The temperature distribution $T(r, \theta)$ within the particle domain $\Omega = \{(r, \theta) : 0 \leq r \leq R; 0 \leq \theta \leq 2\pi\}$ is governed by the Laplace equation as:

$$\begin{cases} \kappa \Delta T = 0 & \text{in } \Omega \\ \kappa \dfrac{\partial T}{\partial n} = q(\theta) & \text{on } \partial\Omega \end{cases} \tag{34}$$

where κ is the thermal conductivity; $\partial\Omega$ denotes the boundary (circumference) of the particle; and $\partial T / \partial n$ is the temperature gradient along the normal direction to the boundary. Then the temperature at any point $(r, \theta) \in \Omega$ can be expressed as

$$T(r, \theta) = -\frac{R}{2\pi\kappa} \int_0^{2\pi} q(\phi) \ln\left[1 - 2\frac{r}{R}\cos(\theta - \phi) + \left(\frac{r}{R}\right)^2\right] d\phi + T_o, \qquad (r, \theta) \in \Omega \tag{35}$$

where T_o is the temperature at the centre, i.e. $T_o = T(0, 0)$.

The solutions (35) are in integral form which provide an explicit formulation to evaluate the temperature distribution over the particle when the input heat flux along the boundary is given.

The temperature distribution along the i-th contact arc is given by

$$T_c^i(\theta) = -\frac{R}{\pi\kappa}\sum_{j=1}^{n}\int_{-\alpha_j}^{\alpha_j} q_j(\phi)\ln\left|\sin\frac{\theta-\phi-\theta_j}{2}\right|d\phi + T_o \quad (\theta_i-\alpha_i \leq \theta \leq \theta_i+\alpha_i)$$

(36)

Define T_i and Q_i respectively as the average temperature and the resultant flux on the i-th arc and further assume that $q_i(\theta)$ is constant. Then T_i can be obtained as

$$T_i = \sum_{j=1}^{n}\left[-\frac{Q_j}{4\pi\kappa\alpha_i\alpha_j}\int_{-\alpha_i}^{\alpha_i}\int_{-\alpha_j}^{\alpha_j}\ln\left|\sin\frac{\Delta\theta_{ij}+\theta-\phi}{2}\right|d\phi d\theta\right] + T_o$$

(37)

or

$$T_i = \sum_{j=1}^{n}h_{ij}Q_j + T_o \qquad (i=1,\ldots,n)$$

(38)

where

$$h_{ij} = h_{ji} = -\frac{1}{4\pi\kappa\alpha_i\alpha_j}\int_{-\alpha_i}^{\alpha_i}\int_{-\alpha_j}^{\alpha_j}\ln\left|\sin\frac{\Delta\theta_{ij}+\theta-\phi}{2}\right|d\phi d\theta > 0$$

(39)

With the introduction of the particle (element) temperature vector $\mathbf{T}_e = \{T_1, \ldots, T_n\}^T$, the heat flux vector $\mathbf{Q}_e = \{Q_1, \ldots, Q_n\}^T$, the particle (element) thermal resistance matrix $\mathbf{H}_e = \{h_{ij}\}_{n\times n}$, and $\mathbf{e} = \{1, \ldots, 1\}^T$, Eq. (38) can be expressed in matrix form as

$$\mathbf{T}_e - \mathbf{e}T_o = \mathbf{H}_e\mathbf{Q}_e$$

(40)

This is the heat conduction equation of the particle in terms of thermal resistance: the temperatures at the n contact zones, relative to the average temperature T_0, can be obtained when the fluxes $\mathbf{Q}_e$ are known. The inverse form of Eq. (40) reads

$$\widehat{\mathbf{K}}_e(\mathbf{T}_e - \mathbf{e}T_o) = \mathbf{Q}_e \qquad (\widehat{\mathbf{K}}_e = \mathbf{H}_e^{-1})$$

(41)

In both Eqs. (40) and (41), the average temperature T_o can be treated as a unknown internal variable which can be obtained by a linear combination of the discrete boundary temperature $\mathbf{T}_e$ as

$$T_o = \mathbf{g}_e^T\mathbf{T}_e/\kappa_e \qquad (\mathbf{g}_e = \widehat{\mathbf{K}}_e\mathbf{e}, \quad \kappa_e = \mathbf{e}^T\widehat{\mathbf{K}}_e\mathbf{e})$$

(42)

Eliminating T_o from Eq. (41) based on relation (42), we have

$$\mathbf{K}_e\mathbf{T}_e = \mathbf{Q}_e$$

(43)

where

$$\mathbf{K}_e = \widehat{\mathbf{K}}_e - \mathbf{g}_e \mathbf{g}_e^T / \kappa_e$$

is the heat conductivity matrix of the particle.

Equation (43) is the heat conduction equation in discrete form for the particle, which is termed the *discrete thermal element*. It has an identical form as a thermal finite element. Thus the subsequent procedure to model heat conduction in the particle system can follow the same procedure as those of the conventional finite element analysis.

This discrete thermal element approach provides a simple and accurate heat conduction model for a circular particle in which the temperature field within the particle is fully resolved, which is a distinct advantage over the existing isothermal models.

In the discrete thermal element, the temperature distribution in a particle is a linear superposition of the contributions from all the heat fluxes at the thermal contact zones. Specifically, the temperature at the i-th zone, T_i, depends not only on the flux Q_i of the zone, but also on other fluxes Q_j. This coupling effect is accounted for by the off-diagonal terms, h_{ij}, in the thermal resistance matrix $\mathbf{H}_e$. The numerical evaluation conducted in [14] shows that a typical value of h_{ij} is about 10 times smaller than that of the diagonal terms h_{ii}, which implies that the coupling effect between different zones is fairly weak. This observation promotes the development of a simplified version of the discrete thermal element formulation, termed the pipe-network model, in [15].

In the pipe-network model, the off-diagonal terms in the thermal resistance matrix $\mathbf{H}_e$ is neglected such that

$$\bar{\mathbf{H}}_e = \text{diag}\{h_{ii}\}$$

Then the original equations (40) are fully decoupled:

$$T_i - T_o = h_{ii} Q_i \qquad (i = 1, \ldots, n) \tag{44}$$

The resulting decoupled thermal equations can be conceptually represented by a simple star-shaped 'pipe' network model, as shown in Figure 3. For an individual pipe i, the corresponding thermal resistance R_i and conductivity k_i are given by

$$R_i = h_{ii}; \qquad k_i = 1/R_i = 1/h_{ii} \tag{45}$$

and Eq. (44) can be rewritten as

$$k_i (T_i - T_o) = Q_i \qquad (i = 1, \ldots, n) \tag{46}$$

In this model, T_o plays a central role. If no external heat source is applied, the net flux at the centre must equal zero due to the heat flux equilibrium requirement $\sum Q_i = 0$. Then Eq. (42) can be further simplified as

$$T_o = \sum_{i=1}^{n} (k_i T_i) \Big/ \sum_{i=1}^{n} k_i \tag{47}$$
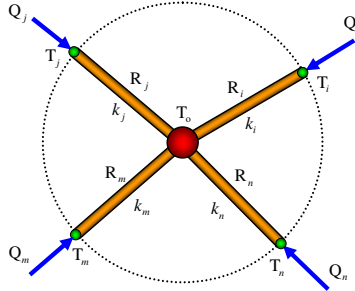
Fig. 3 Pipe-network model

With the pipe-network model, the transient analysis can be readily performed.

The governing equation for the transient heat conduct analysis of a solid is expressed as

$$\rho c_p \dot{T} + \kappa \Delta T = 0 \tag{48}$$

where ρ and c_p are the density and the specific heat capacity of the solid, respectively; $\dot{T} = \partial T / \partial t$ with t being the time.

Within the pipe-network framework, the corresponding discrete version of the transient equation (48) for the i-th particle can be expressed as

$$C_i \dot{T}_i^o + \sum_{j=1}^{n} Q_{ij} = 0 \tag{49}$$

where Q_{ij} are the internal heat fluxes associated with the particle defined by

$$Q_{ij} = k_{ij}(T_j^o - T_i^o) \tag{50}$$

and C_i is the total heat capacity of the particle, given by

$$C_i = \pi \rho c_p R_i^2$$

The global system of equations can be assembled as

$$\mathbf{C}\dot{\mathbf{T}}^o(t) + \mathbf{K}_g \mathbf{T}^o(t) = \mathbf{Q}(t) \tag{51}$$

where the global heat capacity matrix $\mathbf{C} = \text{diag}\{C_i\}$ is a diagonal matrix, $\mathbf{K}_g$ is the global stiffness matrix, and $\mathbf{T}^o = \{T_1^o, \ldots, T_m^o\}^T$ is the average temperature vector of the particles. The system can be solved either explicitly or implicitly.

The formulation of the pipe-network model is compatible with that of the Discrete Element Method, which makes the thermal and mechanical coupling possible.

5 Fluid-Magnetic-Particle Interactions

The fluid-magnetic-particle interaction phenomenon exists in MR fluids. Numerical simulations of MR fluids require an accurate and computationally efficient approach to fully account for magnetic, hydrodynamic and contact interactions. Firstly, the scheme to be employed should be able to effectively model contact phenomena between the magnetizable particles during the evolution of the magnetic micro-structure. The Discrete Element Method described in Section 2 is suitable for this purpose. Secondly, the interaction between the magnetic particles and the carrier fluid can be effectively modelled by the Lattice Boltzmann Method outlined earlier. Special attention in this section will be given to the calculation of magnetic inter-actions. The full version of the modelling methodology is reported in [23] for 2D cases and [24] for 3D cases.

5.1 Magnetic Forces

The magnetic interaction in an MR fluid can be treated as a magnetostatic problem, which is described by Laplace's equation subject to appropriate boundary conditions. The magnetic forces are resolved by formulating the Maxwell stress tensor from the resultant field. The solution procedure is outlined below, based on the work of [26].

Let $\mathbf{H}$ and $\mathbf{B}$ denote the magnetic field intensity and flux density, respectively. For a linear isotropic medium with the magnetic permeability μ, $\mathbf{H}$ and $\mathbf{B}$ are related by the constitutive equation

$$\mathbf{B} = \mu\mathbf{H} \tag{52}$$

Assume that the external magnetic field $\mathbf{H}_0$ is applied along the z direction with a magnitude H_0, i.e. $\mathbf{H}_0 = H_0\mathbf{z}$, where $\mathbf{z}$ denotes the unit vector of the z-axis. If μ_p and μ_f represent, respectively, the magnetic permeability of the particles and fluid, then the relative susceptibility, χ, and effective susceptibility, χ_e, of the particles are defined as

$$\chi = \frac{\mu_p}{\mu_f} \qquad \chi_e = \frac{3(\chi - 1)}{\chi + 2}$$

5.1.1 Fixed Dipole Model

When an external magnetic field is applied, each particle in an MR fluid is magnetized and acquires a magnetic dipole moment $\mathbf{m}$ which, when ignoring the presence of the other particles, is

$$\mathbf{m} = \frac{4\pi R^3}{3}\frac{3(\chi - 1)}{\chi + 2}\mathbf{H}_0 = C_p\mathbf{H}_0; \qquad m = |\mathbf{m}| = C_p H_0 \tag{53}$$
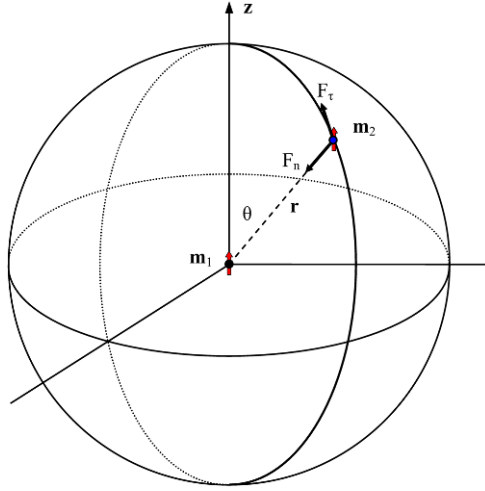
Fig. 4 Magnetic forces on dipole moment $\mathbf{m}_2$ from dipole moment $\mathbf{m}_1$

where $C_p = V_p \chi_e$; $V_p = 4\pi R^3/3$ is the volume of the particle.

Consider one particle with dipole moment $\mathbf{m}_1 = \mathbf{m}$. The magnetic field produced by this dipole at any point (with a relative position vector $\mathbf{r}$ to the dipole) in space can be expressed as [35]

$$\mathbf{H}_1(\mathbf{m}_1, \mathbf{r}) = \frac{1}{4\pi} \frac{3(\mathbf{m}_1 \cdot \hat{\mathbf{r}})\hat{\mathbf{r}} - \mathbf{m}_1}{r^3} \tag{54}$$

where $r = |\mathbf{r}|$ and $\hat{\mathbf{r}} = \mathbf{r}/r$ is the unit vector of $\mathbf{r}$. The corresponding flux density $\mathbf{B}$ is calculated as

$$\mathbf{B}_1(\mathbf{r}) = \mu \mathbf{H}_1(\mathbf{r}) \tag{55}$$

If a second particle of magnetic moment $\mathbf{m}_2 = \mathbf{m}$ is placed in the magnetic field of $\mathbf{m}_1$ as illustrated in Figure 4, the magnetic force, $\mathbf{F}_m$, acting on the second dipole due to the first one can be determined by

$$\mathbf{F}_m(\mathbf{r}) = \nabla(\mathbf{m}_2 \cdot \mathbf{B}_1(\mathbf{r})) \tag{56}$$

with $\mathbf{r} = \mathbf{x}_2 - \mathbf{x}_1$. This force can be expressed more conveniently in a spherical coordinate system (r, θ, φ) with θ and φ being the zenith and azimuth angles, respectively. Particularly, the component of the force in the azimuth angle φ is zero, and the radial and transversal components, $\mathbf{F}_n$ and $\mathbf{F}_\tau$, can be computed as

$$F_n(r, \theta) = -\frac{3\mu}{4\pi} \frac{m_1 m_2}{r^4} [3\cos^2\theta - 1] = -\frac{3\mu}{4\pi} \frac{m_1 m_2}{r^4} \frac{1}{2}[3\cos 2\theta + 1] \tag{57}$$

and

$$F_\tau(r, \theta) = -\frac{3\mu}{4\pi} \frac{m_1 m_2}{r^4} \sin 2\theta \tag{58}$$

Depending on the angle θ, the normal component F_n can be attractive (when $\theta < \theta_c$) or repulsive (when $\theta > \theta_c$), where the critical angle $\theta_c = 54.47°$.

Equations (57) and (58) define the magnetic interaction between any two magnetized particles, which is basically the classic magnetic dipole model, or the fixed dipole model. Owing to its simplicity, this model has been commonly used in modelling MR-fluids, especially when a large number of particles are involved. The pairwise nature of the model also makes it suitable for use within the discrete element modelling framework.

This fixed dipole model is accurate if the separation distance (gap) of two magnetized particles is larger than their diameter $2R$ [26], which suggests a cut-off distance to be used in the later magnetic interaction computation,

$$r_c = 4R \tag{59}$$

However, a large error will be introduced when the separation distance between two particles is less than their radius, $r < R$. This error arises mainly from the strong interaction between the two magnetized fields of the particles, and will reach maximum when the particles touch each other. The numerical investigation performed by [26] shows that for $\chi = 5$, the fixed dipole model underestimates the maximum attraction force by around 35%, while overestimates the maximum repulsive force by 50% or more. The error will become more pronounced for larger susceptibility values.

5.1.2 Mutual Dipole Model

The fixed dipole model discussed above assumes no interactions between the particles' magnetized fields. In fact, the presence of other magnetized particles will increase the magnetization of a particle, thereby enhancing its dipole strength and its interactions with other particles.

If the mutual magnetization between the particles are taken into account, the accuracy of the fixed dipole model may be improved. More specifically, each particle is still viewed as a point dipole but is subjected to an additional secondary magnetization from the other particles' magnetized fields. Note that the magnetization due to the external field is termed the primary magnetization and the magnetization by other particles' magnetized fields is termed the secondary magnetization.

The mutually magnetized moment of particle i, $\mathbf{m}_i$, can be evaluated as

$$\mathbf{m}_i = C_p[\mathbf{H}_0 + \mathbf{H}(\mathbf{x}_i)] \quad (i = 1, \ldots, N) \tag{60}$$

where N is the total number of particles in the system, and $\mathbf{H}(\mathbf{x}_i)$ is the total secondary magnetic field generated by all the other magnetized particles at the centre of particle i,

$$\mathbf{H}(\mathbf{x}_i) = \sum_{j=1, j \neq i}^{N} \mathbf{H}_j(\mathbf{m}_j, \mathbf{r}_{ij}) = \sum_{j=1, j \neq i}^{N} \frac{1}{4\pi} \frac{3\hat{\mathbf{r}}_{ij}(\mathbf{m}_j \cdot \hat{\mathbf{r}}_{ij}) - \mathbf{m}_j}{r_{ij}^3} \qquad (61)$$

with $\mathbf{r}_{ij} = \mathbf{x}_i - \mathbf{x}_j$; $r_{ij} = |\mathbf{r}_{ij}|$; $\hat{\mathbf{r}}_{ij} = \mathbf{r}_{ij}/r_{ij}$.

Equations (60) and (61) define a $3N \times 3N$ linear system of equations with $\mathbf{m}_i$ unknown variables. After all the magnetic moments are solved, the magnetic forces between the particles can be determined by the fixed dipole model using these total magnetization moments. This is the idea behind the so-called mutual dipole model [26].

Nevertheless, the computational cost associated with the solution of the linear system of equation (61) for systems involving a large number of particles can be substantial, and in particular, the solution needs to be performed at every time step of the simulation. In the present work, the classic Gauss–Seidel algorithm is employed to iteratively solve the equations.

Let $\mathbf{m}_i^k$ be the approximate values at the k-th iteration, and $\mathbf{m}_i^0$ be a given initial values. Then at the $k + 1$-th iteration $\mathbf{m}_i$ is computed as

$$\mathbf{m}_i^{k+1} = C_p \left[\mathbf{H}_0 + \sum_{j=1}^{i-1} \mathbf{H}_j(\mathbf{m}_j^{k+1}, \mathbf{r}_{ij}) + \sum_{j=i+1}^{N} \mathbf{H}_j(\mathbf{m}_j^k, \mathbf{r}_{ij}) \right]; \quad k = 0, 1, 2, \dots$$

$$(62)$$

where $\mathbf{m}_i$ at the previous step serves as the initial value for the current step. As the time step is usually very small, it is a very good initial value and thus the convergence of the iterative scheme is rapid. The numerical tests conducted have shown that the above scheme is very effective, and a solution accuracy of 10^{-5} can be generally achieved in no more than three iterations.

Our numerical investigations show that using this mutual dipole model for two particles in contact, the upper limit of the maximum increased magnetic moment is 33.33% for a perfectly magnetized material ($\chi = \infty$), which gives a 77.78% increase of the attraction force; while the upper limit of the maximum decreased magnetic moment is 11.11% which results in a 20.99% decrease of the repulsive force. The effect is even more significant for a longer chain of particles.

However, the exact maximum force between two particles in contact is larger than that predicted by the mutual dipole model. Particularly, it is infinite when $\chi = \infty$.

Further improvement to the mutual dipole model has been undertaken by [26]. After the total magnetized moments are obtained, the force between any two particles is calculated by using the two-body exact solution, a special case of the general solution to multiple particle problems [3]. Although some improvement is achieved, the exact solution is still not obtained since the two-body solution is not exact in general multiple particle cases. More importantly, from a computational point of view, this version of the mutual dipole model loses its original simplicity as a result of the substantial computational cost involved in the incorporation of the two-body exact solution.

In view of the difficulties discussed above, a better approach for improving the accuracy but retaining the computational simplicity of the fixed or mutual dipole model, as proposed by [27], is to use some empirical formulae to describe the magnetic interaction when the particles are close to each other. However, the procedure involves substantial pre-computations for different susceptibility values and different relative positions between two particles.

5.2 Fluid, Magnetic and Particle Coupling

The fluid field is governed by the lattice Boltzmann equation (4) and the particle dynamics is accounted for by the Discrete Element Method. The coupling between the magnetized particles and the carrier fluid is realised through the hydrodynamic and magnetic interactions as

$$\mathbf{M\ddot{u}} + \mathbf{C}_d\mathbf{\dot{u}} = \mathbf{F}_m + \mathbf{F}_f + \mathbf{F}_c \tag{63}$$

which is solved by the central difference algorithm.

6 Numerical Illustration

To assess the applicability of the proposed approach, some numerical experiments will be performed in this section.

6.1 Example 1: Simulation of Particle Transport in a Vacuum Dredging System

The combined Lattice Boltzmann and the Discrete Element procedure described in Section 3 is employed to model a vacuum dredging system for mineral recovery. This recovery operation uses a suction process to extract rock fragments. The system consists of a rigid pipe connected to a slurry transport system, which is typically powered by a gravel pump. The gravel is transported to the pipe entrance via hydraulic entrainment.

The front view of the problem is illustrated in Figure 5, where the suction pipe has an internal diameter of 101 mm and a tube thickness of 16 mm. The gravel is initially confined to a cylindrical region called the gravel bed of 300 mm in diameter and 70 mm in depth. The gravel particles are made of quartz and are assumed to be spherical with diameter in the range of 6–12 mm. A total of 5086 particles are randomly packed using the packing algorithm developed in [19] with an initial porosity of approximately 50%. Full gravity ($g = 9.81$ m/s^2) is applied. The
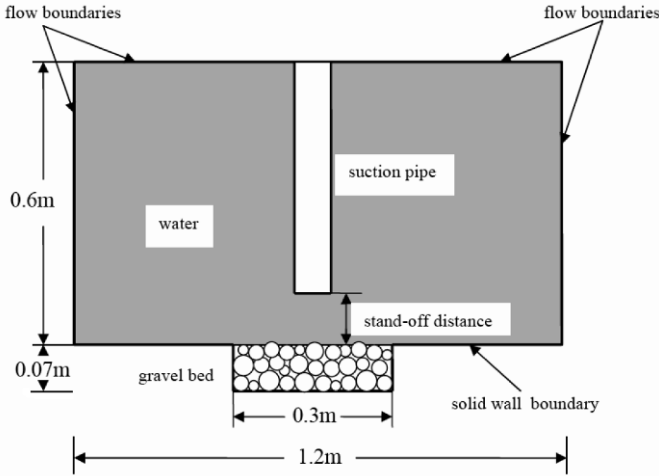
Fig. 5 The front view of the problem geometry

fluid inside the suction pipe is water and is expected to be fully turbulent, thereby the Large Eddy Simulation based Smagorinsky turbulence model is adopted with the Smagorinsky constant $S_c = 0.1$. The following parameters are chosen: particle density $\rho_s = 2650$ kg/m^3, normal contact stiffness $k_n = 5 \times 10^8$ N/m, contact damping ratio $\xi = 0.5$ and time step factor $\lambda = 0.1$, which gives a time step of $\Delta t_D = 1.16 \times 10^{-5}$ for the Discrete Element simulation of the particles. The fluid domain is divided into regular lattice with lattice spacing $\Delta x = 2.5$ mm. The fluid properties are those of water at room temperature, i.e. density $\rho = 1000$ kg/m^3 and kinematic viscosity $\nu = 10^{-6}$ m^2/s. A complete simulation is achieved with $\tau = 0.50002$. This gives a time step $\Delta t = 4.17 \times 10^{-5}$ s and thus the corresponding lattice speed $c = 60$ m/s.

The boundary conditions are set as follows. Except for the bottom of the gravel bed which is a solid stationary wall, the others are flow boundaries. A constant pressure boundary condition with $\rho_{in} = \rho$ is imposed at the inlet walls, and a smaller pressure with $\rho_{out} = 0.975\rho$ is applied to the outlet of the pipe. The flow is therefore driven by the pressure difference between the inlet and outlet.

The relevant laboratory test has also been performed. During the test, video footage is captured using a high speed digital camera. Image processing is used to provide an indication of the gravel velocity history during the test. The final excavation profile and gravel volume removed during the test are also recorded.

Figure 6 shows the images of the gravel motion at the start, during and towards the end of the experiment and simulation, respectively.

Of greater importance are the flow velocity at the pipe outlet, the total weight of the gravel particles removed and the excavation profile. The calculated values are compared with those observed from experimentation. The predicted average velocity on the exit plane of the suction pipe is approximately 0.99 m/s, which agrees
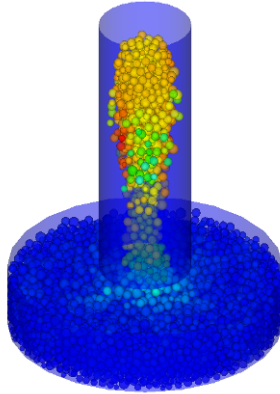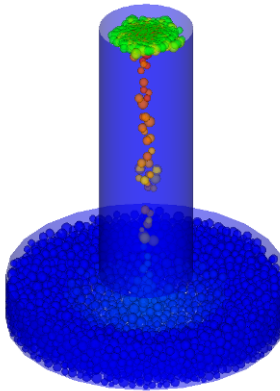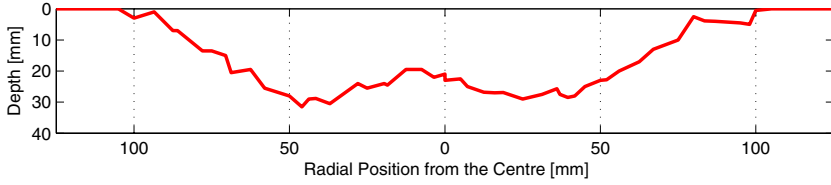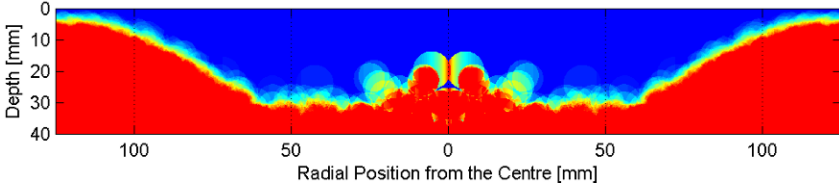
(a)
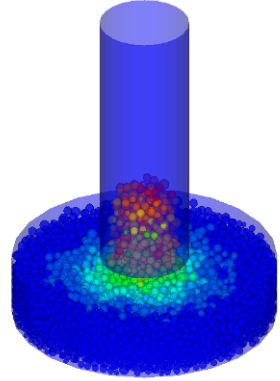
(b)

(c) Gravel motion during the test

(d)

(e)

(f)

Fig. 6 Gravel motion at three stages of test and simulation: at the start of the test (a) and simulation (b); during the test (c) and simulation (d); towards the end of the test (e) and simulation (f)

(a) Excavation profile of the test

(b) Excavation profile of the simulation

Fig. 7 Excavation profiles of the experiment and simulation

well with the measured value (1.05 m/s). A volume of 678341 mm^3 of gravel is removed in the test, which weighs approximately 1.09 kg (assuming a bulk density of 1600 kg/m^3), while 1110 particles, weighting 1.22 kg in total, is excavated in the simulation. The final excavation profiles, measured respectively from experimentation and simulation, at the gravel bed are illustrated in Figure 7. Note that the excavation profile for the simulation is obtained by a radial mapping of all the particles onto the cross section and then rotating about the central axis to create an axisymmetrical profile to facilitate the comparison with the experiment.

The simulated maximum fluid velocity is $v_{max} = 1.36$ m/s at the pipe outlet (with the characteristic length $L = 0.101$ m). Thus the maximum Mach number and Reynolds number are therefore estimated as

$$Ma = \frac{v_{max}}{c} = 0.0226$$

$$R_e = \frac{v_{max}L}{\nu} = 137360$$

The Mach number indicates that the results obtained are reasonably accurate.

It can be seen that the overall correspondence between numerical results and experimental measurements is good.

6.2 Example 2: Simulation of Heat Transfer in a Packed Bed

The problem considered is a randomly packed particle bed of dimensions 0.5×1.0 m. The initial temperature of the 512 particles is set in the range of $[20, 100]°$C. A hot gas $(100°$C) flow is introduced from the bottom of the bed throughout the simulation, while the other boundaries are fully insulated. Full gravity is applied.

To simulate the velocity and temperature fields of this moving particle system with heat transfer, the coupled procedures proposed in this work can be adopted: the gas-particle interaction is modelled by the coupled Lattice Boltzmann and the Discrete Element Methods; while the gas-thermal and particle-thermal interactions are simulated jointly by the Thermal Lattice Boltzmann Method and the Discrete Thermal Element Method.

The physical properties are chosen as: for particles, radius $R = 1-2$ mm, density $\rho_s = 2500$ kg/m^3, heat capacity $c_s = 150$ J/kgK, thermal conductivity $k_s = 35$ W/mK; whereas for the gas, density $\rho_f = 1.0$ kg/m^3, kinematic viscosity $\nu = 10^{-5}$ m^2/s, heat capacity $c_f = 1005$ J/kgK and thermal conductivity $k_f = 0.024$ W/mK. The fluid domain is divided into a 250×500 square lattice with lattice spacing $\Delta x = 2$ mm. The initial packing of the particles is generated using the packing algorithm proposed in [8].

Figures 8(a)–(d) and 9(a)–(d) show snapshot images of the velocity and temperature field evolution. It can be seen that the initially motionless particles start to move upwards when the hydrodynamic forces counteract the gravitational forces acting on the particles. when the velocity of the particles is low, most of the particles are in contacts and the mechanism of conductive heat transfer is significant. As the the particles moves away from each other, the convective transfer of the particles with the surrounding gas becomes dominant. Meanwhile, the particles close to the hot gas inlet (the bottom bed) get heated first and then move upwards, while the particles with lower temperatures move downwards to pick up heat. The circulation patterns of the particles and gas can be clearly seen from the pictures.

6.3 Example 3: Simulation of a Magnetorheological Fluid

A two-stage numerical experiment will be performed for an MR fluid. The simulation involves, at the first stage, the microstructure evolution of the MR fluid with four different particle concentration fractions under the action of an applied magnetic field; and at the second stage, the application of the particle chains established at the first stage as the initial configuration to investigate the rheological properties of the MR fluid under different shear loading conditions.

A representative volume element (RVE) of the MR fluid system to be investigated is chosen to be a rectangular cuboid domain, $0.2 \times 0.05 \times 0.05$ mm, parallel to the axes of a Cartesian coordinate system. As shearing loadings will be applied in the x-direction at the second stage, this dimension is chosen to be the largest for achieving a higher accuracy. The RVE is filled with a Newtonian fluid of dynamic
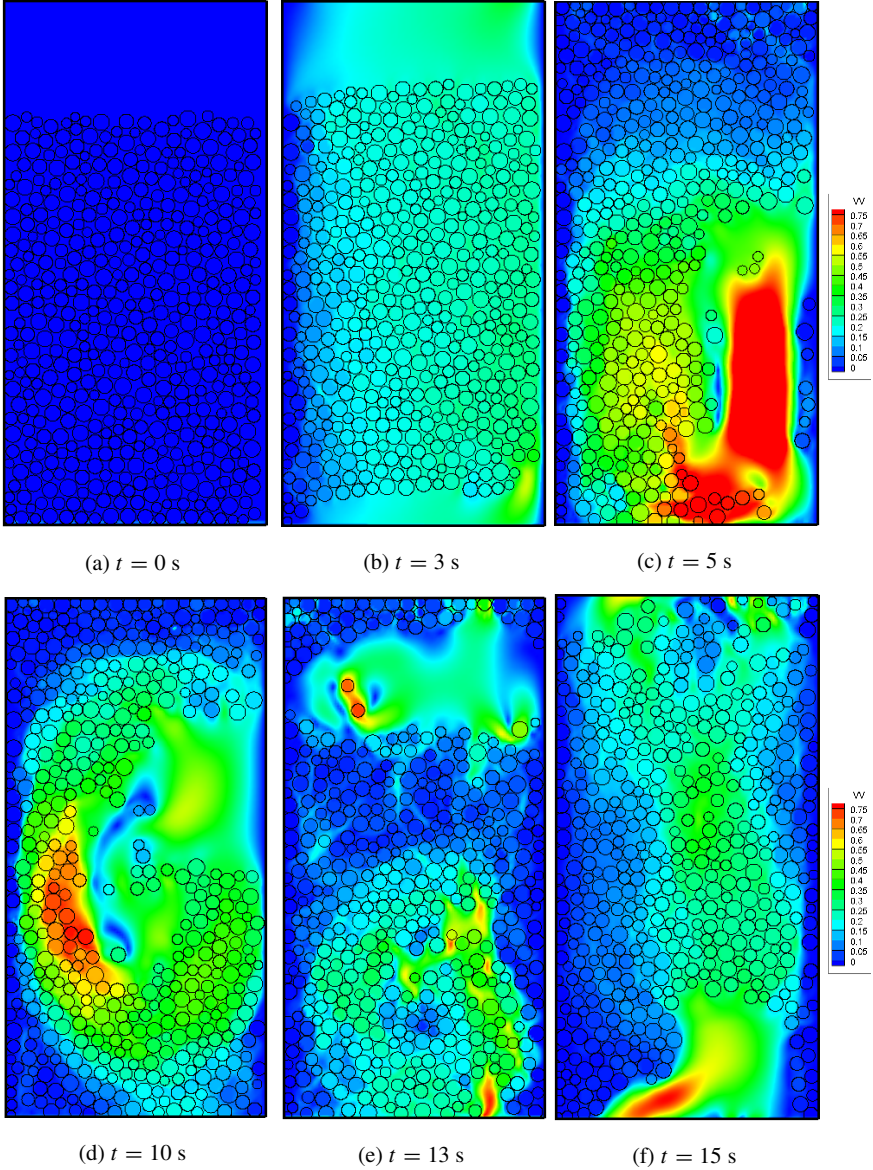
(a) $t = 0$ s   (b) $t = 3$ s   (c) $t = 5$ s

(d) $t = 10$ s   (e) $t = 13$ s   (f) $t = 15$ s

Fig. 8 Velocity contours at six time instants

viscosity $\eta = 0.1$ Pa·s and density $\rho_f = 1000$ kg/m^3 in which spherical magnetiz-able particles are dispersed. The particles are randomly distributed with an identical radius $R = 2$ μm and density $\rho_p = 7\rho_f$. The Young modulus of the particles is set to $E = 10$ GPa, and the Poisson ratio is 0.3. The permeability of the fluid is that of a free space, i.e. $\mu_f = 4\pi \times 10^{-7}$ N/A^2, whereas $\mu_p = 2000\mu_f$ is chosen for the

(a) $t = 0$ s   (b) $t = 3$ s   (c) $t = 5$ s

(d) $t = 10$ s   (e) $t = 13$ s   (f) $t = 15$ s
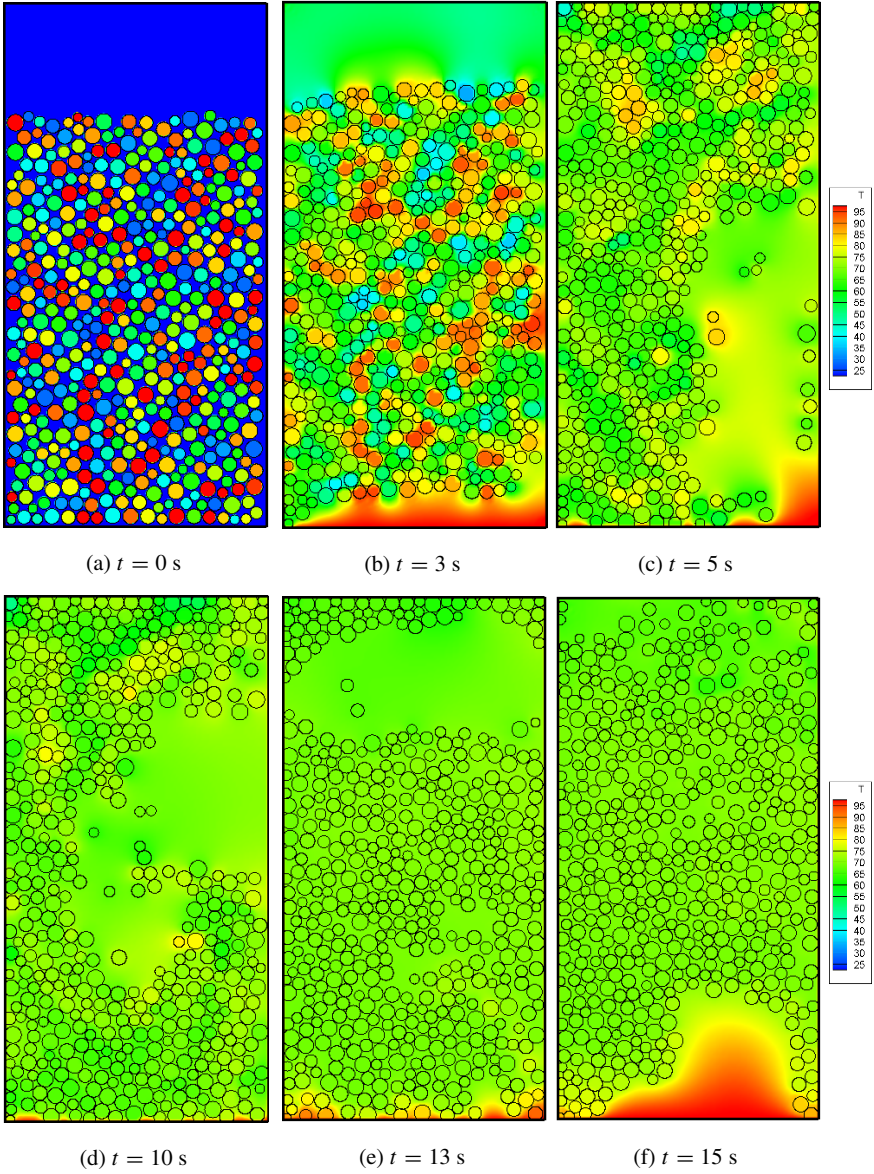
Fig. 9 Temperature contours at six time instants

particles, corresponding to $\chi = 2000$. An external uniform magnetic field is applied in the z-axis direction with a magnitude of $H_0 = 1.33 \times 10^4$ A/m.
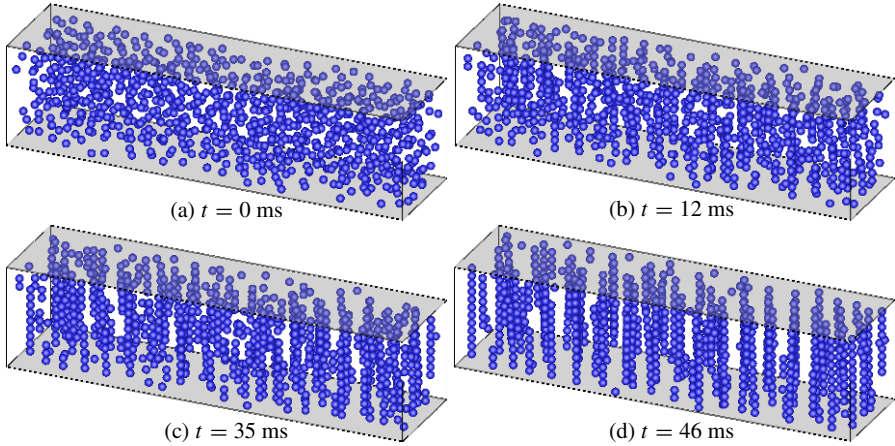
(a) $t = 0$ ms

(b) $t = 12$ ms

(c) $t = 35$ ms

(d) $t = 46$ ms

Fig. 10 Particle dynamics evolution: 5% volume fraction

(a) $t = 0$ ms

(b) $t = 8$ ms

(c) $t = 19$ ms

(d) $t = 33$ ms
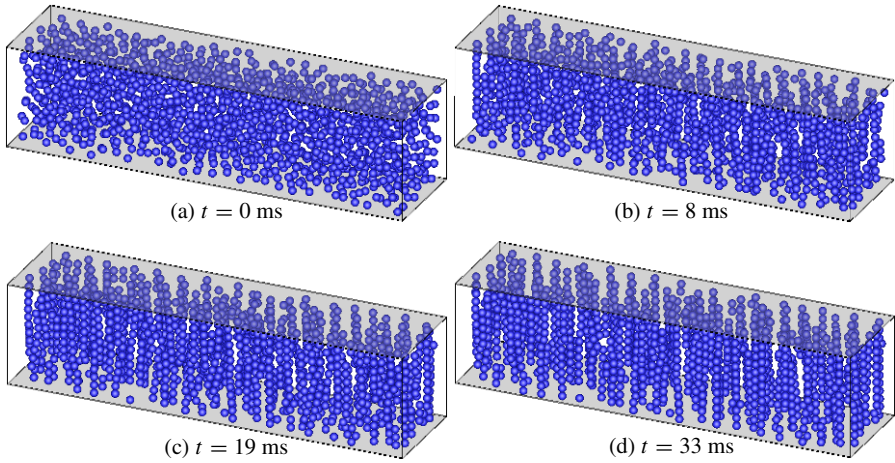
Fig. 11 Particle dynamics evolution: 10% volume fraction

6.3.1 Particle Chain Formation

The particle chain formation under the action of the external magnetic field is simulated for four different samples of the fluid with 5, 10, 20 and 30% particle volume fractions, which correspond to 746, 1492, 2984 and 4476 particles respectively. The evolution of the particle dynamics is solved in the context of the discrete element method in which the magnetic forces are described by the mutual dipole model; the hydrodynamic forces are approximated with the Stokes formula since the fluid field is not resolved at this stage; and the contact forces are evaluated by the Hertzian model. Periodic boundary conditions are imposed on the RVE for the particles in all the directions, i.e. if a particle moves out of the RVE from one end, it re-enters from
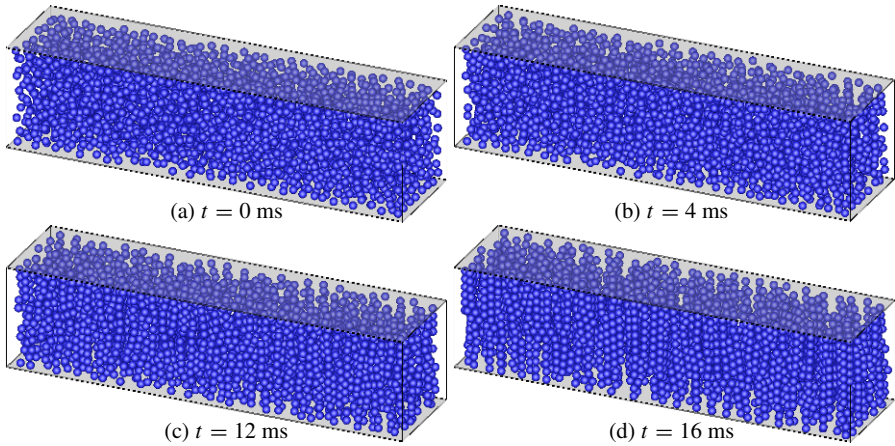
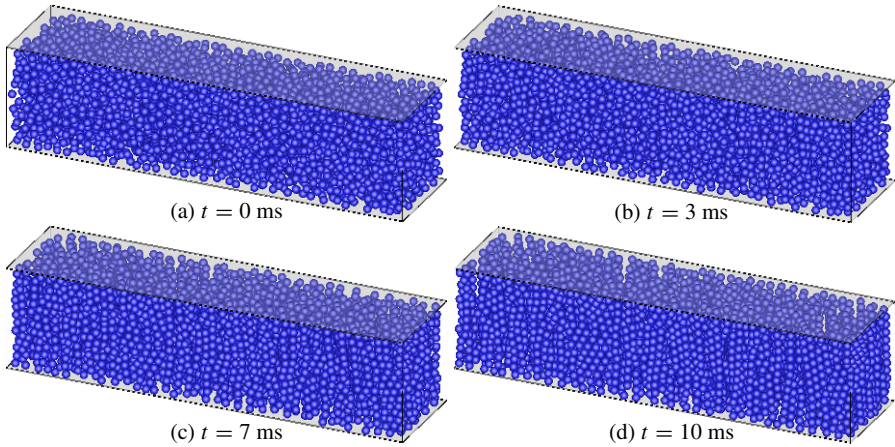**Fig. 12** Particle dynamics evolution: 20% volume fraction

Fig. 13 Particle dynamics evolution: 30% volume fraction

the other end. The time step size used in the central difference time integration is 1.36×10^{-8} s. The simulation is terminated when the system reaches a steady state.

The dynamic evolution of the entire system is monitored by the history plot of the total kinetic energy of the particles. A suitably small value of the total kinetic energy indicates that a steady state is reached. With this information, the response time of the MR fluid system can also be identified.

Figures 10–13 depict the microstructure evolution of the particles at four time instants for the four different particle concentrations. It can be seen that with the application of the magnetic field, the particles become magnetized and acquire a magnetic dipole moment. Due to dipolar interactions, the particles aggregate to form short fragmented chains. As time progresses, these short chains merge together to
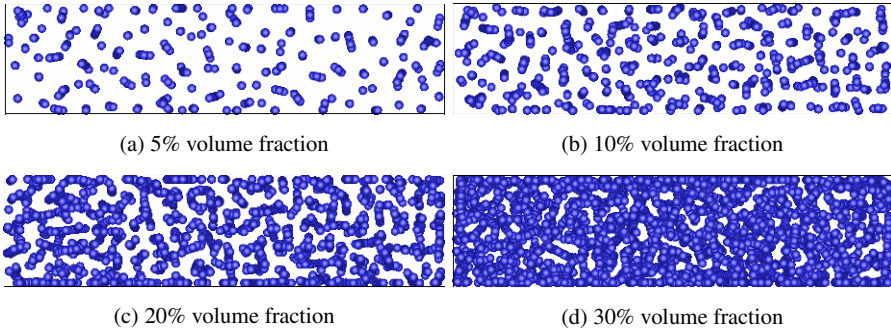
(a) 5% volume fraction

(b) 10% volume fraction

(c) 20% volume fraction

(d) 30% volume fraction

Fig. 14 Top views of final formed particle chains for four volume fractions

form longer chains that align in the direction of the applied magnetic field. Theoretically, the final chain structure corresponds to a (possibly local) minimum energy state.

The particle concentration in the MR fluid has significant effect on the formed chain configurations. For a lower volume fraction, greater mobility of the particles results in straighter chains of single particle width aligned with the applied magnetic field; while for a higher volume fraction, less mobility of the particles make it difficult to form straight chains. Some of the chains tangle with other chains to form multiple particle width strands or clusters. This is illustrated in Figure 14, where the top views of the final particle chains are displayed.

Figure 15 is the time history plot (truncated after 25 ms) of the averaged kinetic energy per particle for the four particle volume fractions. The kinetic energy rapidly reaches the peak value within a few milliseconds, indicating an active particle motion at the initial particle aggregation. The subsequent decrease of kinetic energy corresponds to a further growth of particle chains until the final stable configurations are achieved. The local spikes, notably for the lower volume fractions (5 and 10%), represent merging of shorter chains. There are far fewer spikes in the higher volume fractions (20 and 30%) which indicates a continuous formation/merging of the (shorter) chains.

The simulations have establish that the times for the systems to approach a steady state, i.e. the response time, are approximately inversely proportional to the particle volume fractions, which are about 46, 33, 16 and 10 milliseconds respectively for 5, 10, 20 and 30% volume fractions. Clearly the steady state is reached faster for a higher volume concentration of the particles, as expected.

Additional simulations have also been performed for two different intensities of the applied magnetic field, $0.5H_0$ and $2H_0$. Except that a stronger (weaker) magnetic field results in a shorter (longer) response time, the final chain configurations are not much different, implying that the particle volume fraction plays a dominant role in the particle dynamic simulation. In particular, the mutual dipole model, though inaccurate when the particles are very close, may be sufficient if only the microstructure of the particle chains is of interest.
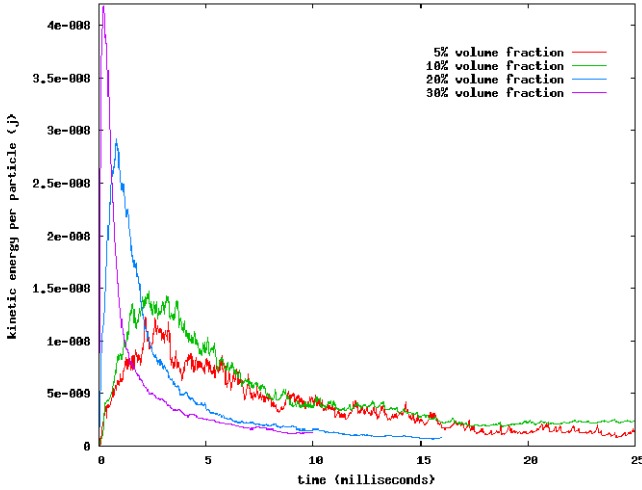
Fig. 15 History plot of the kinetic energy per particle for four different particle volume fractions

6.3.2 Rheological Properties under Shear Loading

As shown in the previous subsection, with the application of an external magnetic field, columnar particle chains are formed which are perpendicular to the direction of the fluid flow in the MR fluid. As a result, the fluid motion is largely restricted. This change in the suspension microstructure greatly alters the rheological properties of the fluid. To examine the MR effect, the following numerical tests are performed to establish the relationship between the applied shear loading and the resulting shear stress or viscosity under different magnetic field strengths.

The steady-state particle chains established at the first stage simulation are applied as the initial configuration of the MR fluid system. In the following simulations, the MR fluid with 10% particle volume fraction investigated in the previous subsection is chosen. The combined LBM and DEM procedure is employed to fully resolve the fluid field and particle-fluid interaction. The fluid domain is divided into a $400 \times 100 \times 100$ cubic lattice with lattice spacing $h = 0.5$ μm. The relaxation time is chosen to be $\tau = 0.75$ to match the viscosity of the fluid, which leads to a time step for the fluid of 2.08×10^{-10} s and a lattice speed $c = 2400$ m/s. The same time step is also used for the particles. The maximum computational Mach number encountered for all the simulations is $M_a = 0.006$, which is much smaller than 1.0, therefore the numerical results are reasonably accurate.

A constant horizontal velocity v_0 in the positive x-direction is applied to the top surface of the RVE, and the equivalent shear rate is $\dot{\gamma} = v_0/W$ with $W = 0.05mm$ the height of the domain. By changing the value of v_0, different shear rates can be applied. Three types of fluid boundary conditions are applied: 'no-slip' for the bottom surface; slip for the front and back surfaces; and periodic for the left and the right surfaces. Special treatment is made to the shared edges and vertices of
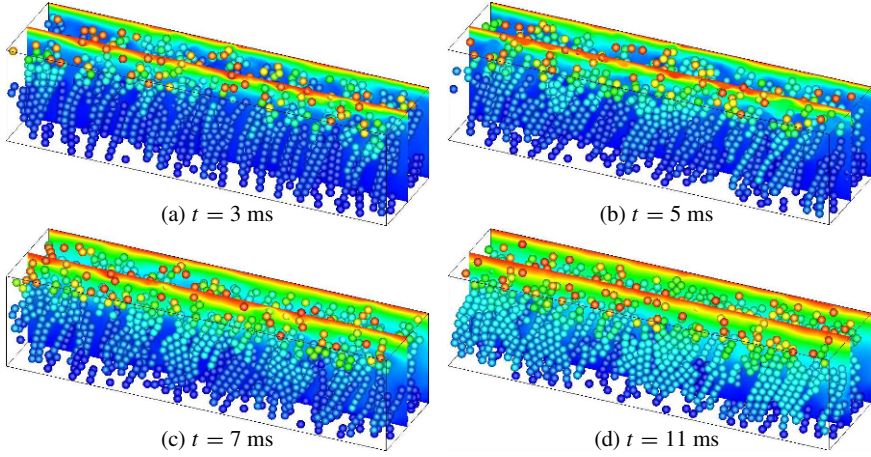
Fig. 16 Four snapshots in a shear mode simulation: $H_0 = 1.33 \times 10^4$ A/m, $\dot{\gamma} = 240$ s^{-1}

the surfaces with different boundary conditions. A pure shear flow case (without particles) is tested to ensure a linear velocity distribution along the z direction and an identical fluid field for all the vertical planes parallel to the x–z plane.

Due to the shear loading applied, the boundary conditions for the particles are slightly modified. The particles are restrained between the top, bottom, front and back surfaces, which is achieved by implementing mechanical contact conditions between the particles and the boundaries. The periodic condition is applied in the x-direction, i.e. the particles are allowed to move out of the RVE from the right surface but re-enter the domain from the left surface. For the magnetic interaction computation, however, the same full periodic conditions as those in the previous particle dynamic simulations are imposed.

During the course of the simulation, the total horizontal shear force, F_s, acting on the top surface is recorded. The final converged value, when divided by the total area, $A = 0.0025$ mm^2, of the top surface, gives the apparent stress $\sigma = F_s/A$. The apparent viscosity is then calculated as $\sigma/\dot{\gamma}$. Seven different shear rates, $\dot{\gamma} = 24, 60, 120, 180, 240, 360, 480$ s^{-1} and three different magnetic intensities $H = 0.5H_0, H_0, 2H_0$, which combine into 21 different cases, are simulated.

Figure 16 depicts the total velocity contour of the MR fluid system (the particles and fluid at two cross-sections) at four time instants for the shear rate $\dot{\gamma} = 240$ s^{-1} and the external magnetic field H_0. These snapshots show a typical shear behaviour of an MR fluid. Under the shear operation, the particles close to the moving top surface break from the chains first (Figure 16a), then the (long) particle chains soon get deformed (Figure 16b), detach from the bottom surface (Figure 16c), and finally break into shorter chains that tend to re-group to form one layer of clusters (Figure 16d). These correspond to a sharp decrease in the shear force at the initial stage and then achieve a steady-state afterwards, as shown in Figure 17.
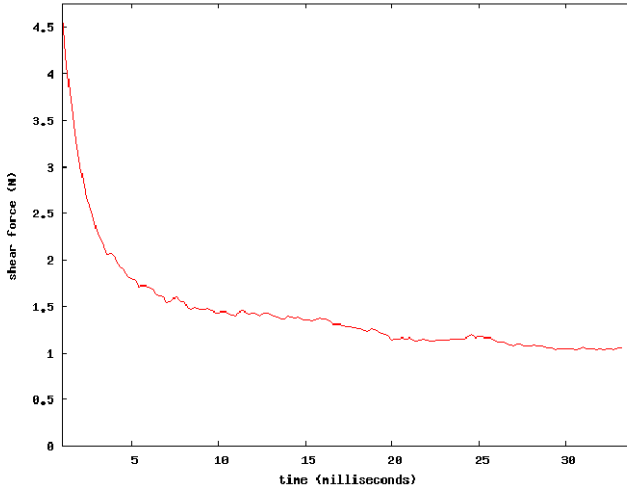
Fig. 17 Shear force history in a shear mode simulation: $H_0 = 1.33 \times 10^4$ A/m, $\dot{\gamma} = 240$ s^{-1}

Figure 18 depicts the shear stress and viscosity as a function of the applied shear rates for three different magnetic strengths. It can be seen that the MR fluid behaves like a Bingham fluid. Figure 18(b) indicates the shear thinning behaviour of the MR fluid, whereby the viscosity upon yielding decreases with the increased shear rate. This phenomenon can be explained by the fact that with increase of the shear rate, the microstructure formed is destroyed rapidly by the increased shear stresses; longer particle chains are broken into shorter chains, which improves the fluidity of the fluid and leads to a decrease in fluid viscosity.

Figure 18 also shows that both apparent viscosity and shear stress increase with increase of the magnetic field strength, as expected, but in a nonlinear fashion, implying that numerical modelling may be an ideal tool to predict the rheological behaviour of MR fluids under a wide range of operational conditions. The magnetic interaction forces between the suspended particles increase with increase of the magnetic field strength, which causes larger resistance to the fluid flow and therefore the MR fluid gains larger viscosity and shear stress. Thus, unlike the particle chain formation, the accuracy of the magnetic interaction models has a major effect on the simulated rheological properties of an MR fluid.

The dynamic yield stress is an important property of MR fluids. It is theoretically defined as the limiting value of the shear stress when the shear rate tends to zero. As observed in [27], it is computationally intensive to undertake the simulations at small shear rates since a large number of time increments have to be performed, especially in three-dimensional situations. The yielding behaviour of the MR fluid is not addressed in this work.
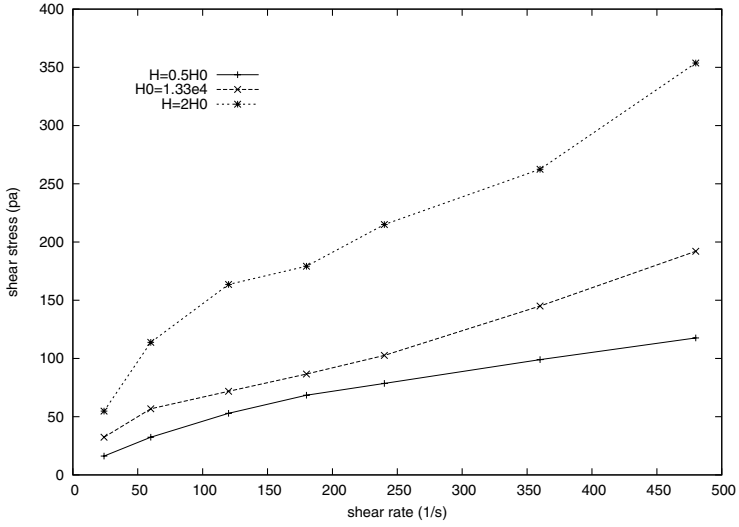
(a) Shear stress versus shear rate
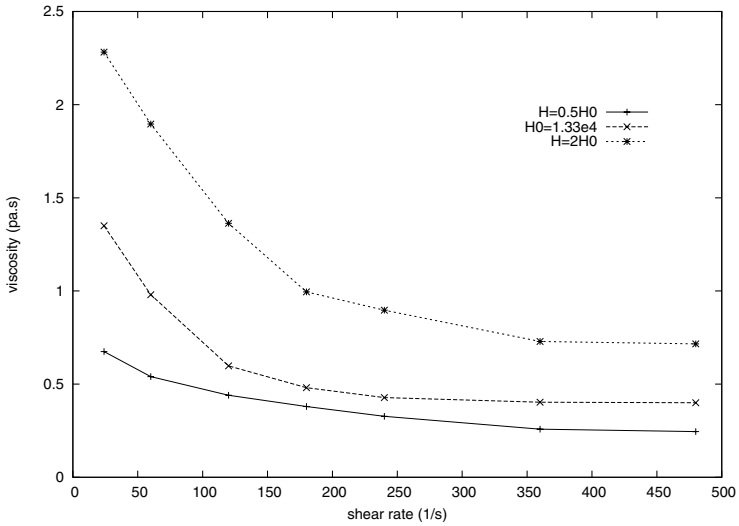
(b) Viscosity versus shear rate

Fig. 18 MR effect under three different magnetic fields

7 Concluding Remarks

The present work has established a computational framework for the effective coupling of multi field interactions in particulate systems, in which the motion of the

particles is simulated by the Discrete Element Method; the mass and velocity field of the fluid flow is modelled by the Lattice Boltzmann Method; the temperature field of the heat transfer is solved jointly by the Discrete Thermal Element Method and the Thermal Lattice Boltzmann Method. The coupling of the hydrodynamic, thermodynamic and magnetic interactions are realised through the force terms. The applicability of the proposed approach has been illustrated via selected numerical examples.

References

1. Aidun, C.K., Lu, Y., Ding, E.G., Direct analysis of particulate suspensions with inertia using the discrete Boltzmann equation. *Journal of Fluid Mechanics*, 373:287–311, 1998.
2. Chen, S., Doolen, G., Lattice Boltzmann method for fluid flows. *Annual Review of Fluid Mechanics*, 30:329–364, 1998.
3. Clercx, H., Bossis, G., Many-body electrostatic interactions in electrorheological fluids. *Physical Review E*, 48(4):2721–2738, 1993.
4. Cook, B.K., Noble, D.R., Williams, J.R., A direct simulation method for particle-fluid systems. *International Journal for Engineering Computations*, 21(2-4):151–168, 2004.
5. Cundall, P.A., Strack, O.D.L., A discrete numerical model for granular assemblies. *Géotechnique*, 29:47–65, 1979.
6. Feng, Y.T., Owen, D.R.J., An augmented spatial digital tree algorithm for contact detection in computational mechanics. *International Journal for Numerical Methods in Engineering* 55:556–574, 2002.
7. Feng, Y.T., Han, K., Owen, D.R.J., Some computational issues on numerical simulation of particulate systems. In *Proceedings of the Fifth World Congress on Computational Mechanics*, H.A. Mang, F.G. Rammerstorfer, J. Eberhardsteiner (eds.), 2002.
8. Feng, Y.T., Han, K., Owen, D.R.J., Filling domains with disks: An advancing front approach. *International Journal for Numerical Methods in Engineering*, 56:699–713, 2003.
9. Feng, Y.T., Han, K., Owen, D.R.J., An advancing front packing of polygons, ellipses and spheres. In *Proceedings of the Third International Conference on Discrete Element Methods*, B.K. Cook and R.P. Jensen (eds.), pp. 93–98, 2002.
10. Feng, Y.T., Owen, D.R.J., A 2D polygon/polygon contact model: Algorithmic aspects. *International Journal for Engineering Computations*, 21:265–277, 2004.
11. Feng, Y.T., Han, K., Owen, D.R.J., An energy based polyhedron-to-polyhedron contact model. In *Proceeding of 3rd MIT Conference of Computational Fluid and Solid Mechanics*, MIT, USA, 14–17 June, 2005.
12. Feng, Y.T., On the central difference algorithm in discrete element modeling of impact. *International Journal for Numerical Methods in Engineering*, 64(14):1959–1980, 2005.
13. Feng, Y.T., Han, K., Owen, D.R.J., Coupled lattice Boltzmann method and discrete element modelling of particle transport in turbulent fluid flows: Computational issues. *International Journal for Numerical Methods in Engineering*, 72(9):1111–1134, 2007.
14. Feng, Y.T., Han, K., Li, C.F., Owen, D.R.J., Discrete thermal element modelling of heat conduction in particle systems: Basic Formulations. *Journal of Computational Physics*, 227:5072–5089, 2008.
15. Feng, Y.T., Han, K., Owen, D.R.J., Discrete thermal element modelling of heat conduction in particle systems: Pipe-network model and transient analysis. *Powder Technology*, 193(3):248–256, 2009
16. Feng, Y.T., Han, K., Owen, D.R.J., Combined three-dimensional Lattice Boltzmann Method and Discrete Element Method for modelling fluid-particle interactions with experimental validation. *International Journal for Numerical Methods in Engineering*, 81(2):229–245, 2010.

17. Han, K., Peric, D., Crook, A.J.L., Owen, D.R.J., Combined finite/discrete element simulation of shot peening process. Part I: Studies on 2D interaction laws. *International Journal for Engineering Computations*, 17(5):593–619, 2000.
18. Han, K., Peric, D., Owen, D.R.J., Yu, J., Combined finite/discrete element simulation of shot peening process. Part II: 3D interaction laws. *International Journal for Engineering Computations*, 17(6/7):683–702, 2000.
19. Han, K., Feng, Y.T., Owen, D.R.J., Sphere packing with a geometric based compression algorithm. *Powder Technology*, 155(1):33–41, 2005.
20. Han, K., Feng, Y.T., Owen, D.R.J., Polygon-based contact resolution for superquadrics. *International Journal for Numerical Methods in Engineering*, 66:485–501, 2006.
21. Han, K., Feng, Y.T., Owen, D.R.J., Numerical simulations of irregular particle transport in turbulent flows using coupled LBM-DEM. *Computer Modeling in Engineering & Science*, 18(2):87–100, 2007.
22. Han, K., Feng, Y.T., Owen, D.R.J., Performance comparisons of tree based and cell based contact detection algorithms. *International Journal for Engineering Computations*, 24(2):165–181, 2007.
23. Han, K., Feng, Y.T., Owen, D.R.J., Modelling of Magnetorheological Fluids with Combined Lattice Boltzmann and Discrete Element Approach. *Communications in Computional Physics*, 7(5):1095–1117, 2010.
24. Han, K., Feng, Y.T., Owen, D.R.J., Three dimensional modelling and simulation of magnetorheological fluids. *International Journal for Engineering Computations*, Published Online: June 28, 2010.
25. He, X., Chen, S., Doolen, G.R., A novel thermal model for the lattice Boltzmann method in imcompressible limit. *Journal of Computational Physics*, 146:282–300, 1998.
26. Keaveny, E.E., Maxey, M.R., Modeling the magnetic interactions between paramagnetic beads in magnetorheological fluids. *Journal of Computational Physics*, 227:9554–9571, 2008.
27. Klingenberg, D., van Swol, F., Zukoski, C., The small shear rate response of electrorheological suspensions. II. Extension beyond the point-dipole limit. *Journal of Chemical Physics*, 94(9):6170–6178, 1991.
28. Ladd, A., Numerical simulations of fluid particulate suspensions via a discretized Boltzmann equation (Parts I & II). *Journal of Fluid Mechanics*, 271:285–339, 1994.
29. Ladd, A., Verberg, R., Lattice-Boltzmann simulations of particle-fluid suspensions. *Journal of Statistical Physics*, 104(5/6):1191–1251, 2001.
30. Noble, D., Torczynski, J., A lattice Boltzmann method for partially saturated cells. *International Journal of Modern Physics C*, 9:1189–1201, 1998.
31. Munjiza, A., Andrews, K.R.F., NBS contact detection algorithm for bodies of similar size. *International Journal for Numerical Methods in Engineering*, 43:131–149, 1998.
32. Perkins, E., Williams, J.R., A fast contact detection algorithm insensitive to object sizes. *International Journal for Engineering Computations*, 12:185–201, 1995.
33. Qian, Y., d'Humieres, D., Lallemand, P., Lattice BGK models for Navier–Stokes equation. *Europhys. Lett.* 17:479–484, 1992.
34. Smagorinsky, J., General circulation model of the atmosphere. *Weather Rev.*, 99–164, 1963.
35. Stratton, J.A., *Electromagnetic Theory*, First Edition. McGraw-Hill Book Company, 1941.
36. Chen, H., Kandasamy, S., Orszag, S., Shock, R., Succi, S., Yakhot, V., Extended Boltzmann kinetic equation for turbulent flows. *Science*, 301:633–636, 2003
37. Williams, J.R., O'Connor, R., A linear complexity intersection algorithm for discrete element simulation of arbitrary geometries. *International Journal for Engineering Computations*, 12:185–201, 1995.
38. Yu, H., Girimaji, S., Luo, L., DNS and LES of decaying isotropic turbulence with and without frame rotation using lattice Boltzmann method. *Journal of Computational Physics*, 209:599–616, 2005.